Available online at www.sciencedirect.com
ScienceDirect
Comput. Methods Appl. Mech. Engrg. 397 (2022) 115144
Computer methods in applied mechanics and engineering
www.elsevier.com/locate/cma

# A study on the approximation power of NURBS and the significance of exact geometry in isogeometric pre-buckling analyses of shells

Bastian Oesterle[a,*], Florian Geiger[b], David Forster[b], Manuel Fröhlich[c], Manfred Bischoff[b]

[a] *Hamburg University of Technology, Institute for Structural Analysis, Denickestraße 17, 21073 Hamburg, Germany*
[b] *University of Stuttgart, Institute for Structural Mechanics, Pfaffenwaldring 7, 70569 Stuttgart, Germany*
[c] *schlaich bergermann partner GmbH, Schwabstraße 43, 70197 Stuttgart, Germany*

Received 8 November 2021; received in revised form 9 May 2022; accepted 15 May 2022
Available online 9 June 2022

**Abstract**

We present a comprehensive study on the approximation power of NURBS and the significance of exact geometry in stability analyses of shells. Pre-buckling analyses are carried out to estimate the critical load levels and the initial buckling patterns. Various finite element solutions obtained with the commercial code ANSYS are compared with solutions from the isogeometric version of the finite element method, using our in-house code NumPro. In some problem setups, the isogeometric shell elements provide superior accuracy compared to standard (as opposed to isogeometric) shell finite elements, requiring only a fractional amount of degrees of freedom for the same level of accuracy. The present study systematically investigates the sources of this superior accuracy of the isogeometric approach. In particular, hypotheses are tested concerning the influence of exact geometry and smoothness of splines.


*Keywords:* Shells; Buckling; Finite element analysis (FEA); Isogeometric analysis (IGA); Exact geometry

## 1. Introduction

In recent years, an increased activity in the scientific field of formulations and discretization methods for shell structures can be observed, see for instance [1–9], among many others. The topic has received a major boost due to the popularity of isogeometric analysis (IGA) [10], since smooth splines are particularly attractive in problems for which the weak form has a variational index of 2 or larger, for instance, the classical Kirchhoff–Love (KL) thin shell model.

Besides this, IGA provides highly promising results in many research areas of computational mechanics, for instance fluid mechanics, fluid structure interaction, structural dynamics and contact. It has also shown great potential in the context of collocation methods. In some applications, IGA seems to be a serious alternative to traditional finite element analysis (FEA) or even superior in terms of accuracy of the results, see for instance [11], among others. But the particular reasons for superior results of IGA in specific problems and aspects are not very well studied so far. Some contributions, like [12], indicate, that so-called $k$-refinement, retaining maximum smoothness

* Corresponding author.
*E-mail address:* bastian.oesterle@tuhh.de (B. Oesterle).

https://doi.org/10.1016/j.cma.2022.115144

of $C^{p-1}$ in order elevation, may lead to superior accuracy compared to classical $h$- or $p$-refinement strategies known from FEA with $C^0$-continuity. But maximum smoothness is not always beneficial. This is particularly the case in problems with very large gradients, as shown in [12], or when locking is pronounced, for instance in the analysis of thin shell structures, as shown in [13–15], among others.

Another frequently mentioned key feature of IGA is the use of "exact" geometry from CAD for simulation in engineering. Besides possible savings in time due to simplified workflows and avoidance of (re-)meshing, a key question is, whether better results can be achieved through better geometry. It may not be possible to provide a general answer to this question, however, in the present work, we present a systematic study on the significance of exact geometry in stability analyses of shells. Already in the introduction of the pioneering work of IGA in 2005 [10] it is stated, that "The geometric approximation inherent in the mesh can lead to accuracy problems. One example of this is in thin shell analysis, which is notoriously sensitive to geometric imperfections". Since this time, stability problems of shell structures employing IGA have not been studied very deeply and corresponding literature is rare. Recent contributions from Leonetti et al. [16] and Guo et al. [17] have to be mentioned. The former contribution deals with Koiter's theory for buckling and initial post-buckling analyses of composite shells using an isogeometric solid-shell formulation. The latter utilized an isogeometric thin shell KL formulation for the study of nonlinear stability analyses of shell structures. Both contributions mention the exact geometry of the discretization, but corresponding effects and implications are not studied in detail.

In the present work, we show for pre-buckling analyses of shells, that isogeometric shell formulations may provide superior accuracy compared to standard (as opposed to isogeometric) shell finite elements in detecting both critical load levels and physical buckling patterns. That is, isogeometric shell formulations may require only a fractional amount of degrees of freedom for the same level of accuracy obtained with a fine finite element mesh. But: What is the reason for these superior results? Is it due to a better approximation of the solution by smooth splines compared to Lagrange/Hermite polynomials? Or is the better, i.e. "exact", geometry within IGA the key factor for the superior results? The aim of this contribution is to answer these questions in a systematic way. The present study does explicitly not cover the aspect of sensitivity to geometric imperfections, which would require both different analysis methods and different considerations.

The paper is organized as follows. Section 2 briefly introduces the definition of critical points and different types of stability analyses. Section 3 provides comprehensive numerical case studies. Effects of solution approximation and geometry approximation are systematically separated. Finally, Section 4 concludes the achieved results and gives an outlook on open issues and potential future developments.

## 2. Critical points and stability

### 2.1. Equilibrium path and tangent stiffness

This chapter gives a short review on static equilibrium paths, critical points and static stability. By definition, a *static equilibrium path* is the locus of all points in an abstract space spanned by a load factor $\lambda$ and the vector $\mathbf{D}$ of degrees of freedom (DOF) for which internal forces $\mathbf{F}_{\text{int}}$ and external forces $\mathbf{F}_{\text{ext}}$ are in static equilibrium,

$$\mathbf{F}_{\text{int}}(\mathbf{D}) = \mathbf{F}_{\text{ext}}(\lambda) = \lambda \mathbf{F}_0. \tag{1}$$

The notation refers to a discrete (or discretized) system and we restrict ourselves to situations, in which the vector of internal forces depends on the state vector (or displacement vector) $\mathbf{D}$ and the external forces exclusively depend on the load factor $\lambda$, but not on the displacements. Formally, the condition of static equilibrium can also be expressed as requiring the residual vector to vanish,

$$\mathbf{R}(\mathbf{D}, \lambda) = \mathbf{F}_{\text{int}}(\mathbf{D}) - \mathbf{F}_{\text{ext}}(\lambda) = \mathbf{0}. \tag{2}$$

Fig. 1 shows the projection of this path into a plane, obtained for a selected displacement degree of freedom $D_i$. It is not necessarily identical to the actual system response for a quasi-static loading. Nevertheless, it is often also referred to as "load–displacement curve". The branch of the equilibrium path starting at the origin is called primary path, whereas other paths branching off are called secondary paths. For systems with $n$ DOF, an equilibrium path can be plotted as the projection of a curve in $\mathbb{R}^{n+1}$-dimensional space onto a curve in $\mathbb{R}^2$.

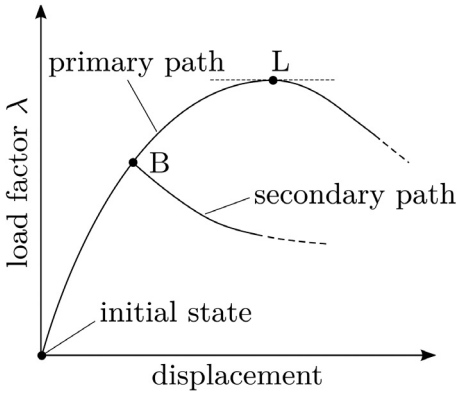


**Fig. 1.** Load–displacement diagram and critical points. B: Bifurcation point, L: Limit point.

Stability characteristics are mainly influenced by the stiffness of a structure. The tangent stiffness is defined by the directional derivative of $\mathbf{R}$ with respect to the displacement vector $\mathbf{D}$. In the given case of loads that are independent of the deformation state, that is non-follower loads or dead loads, the derivative of $\mathbf{F}_{\text{ext}}$ with respect to $\mathbf{D}$ is zero and we obtain

$$\mathbf{K}_{\text{T}} = \frac{\partial \mathbf{R}}{\partial \mathbf{D}} = \frac{\partial \mathbf{F}_{\text{int}}}{\partial \mathbf{D}}. \tag{3}$$

A common definition of stability says that a small perturbation of an equilibrium state does not lead to an excessive dislocation or even the collapse of the structure. A definition of stability referring to the potential energy can be found in [18], among others. Regarding the equilibrium path of conservative systems, the transition from stable to unstable equilibrium occurs at critical points [19]. Consequently, the determination of critical points is of crucial importance.

### 2.2. Classification of critical points

For the time being, we restrict ourselves to load cases with displacement independent (conservative) external forces and load control (as opposed to displacement control or prescribed non-zero displacements). Critical points are classified into limit points (L) and bifurcation points (B) (see Fig. 1). Bifurcation points are associated with the term *buckling* whereas limit points are associated with *snap-through* phenomena. If the load is increased beyond a limit point, the structure dynamically changes to the nearest stable equilibrium point for the same load-level. When reaching a bifurcation point, the system switches to the secondary branch, which may mean immediate collapse but can also be stable, if the secondary branch has a positive stiffness. Corresponding nonlinear analyses, however, are not in the focus here. We merely seek to identify an approximation for the first critical point and the associated buckling mode.

At critical points, the tangent stiffness matrix $\mathbf{K}_{\text{T}}$ is singular, which results in a vanishing determinant

$$|\mathbf{K}_{\text{T}}| = 0. \tag{4}$$

The stiffness matrix then has at least one zero eigenvalue $\kappa = 0$. The eigenvalue problem

$$(\mathbf{K}_{\text{T}} - \kappa \mathbf{I})\, \boldsymbol{\Phi} = \mathbf{0} \quad \overset{\kappa=0}{\Rightarrow} \quad \mathbf{K}_{\text{T}} \boldsymbol{\Phi} = \mathbf{0} \tag{5}$$

provides the *buckling vector* $\boldsymbol{\Phi}$, which identifies the direction in which stiffness is zero. Eqs. (4) and (5) are valid for both types of critical points. To distinguish between limit and bifurcation points, [20] considers the equilibrium path, expressed by the residual force $\mathbf{R}$, as a function of the variables $\lambda$ and $\mathbf{D}$ which in turn depends on a path parameter $s$

$$\mathbf{R}\left(\mathbf{D}\left(s\right), \lambda\left(s\right)\right) = \mathbf{0}. \tag{6}$$

Differentiating Eq. (6) w.r.t. $s$ yields

$$\frac{\partial \mathbf{R}}{\partial s} = \underbrace{\frac{\partial \mathbf{R}}{\partial \mathbf{D}}}_{\mathbf{K}_\mathrm{T}} \frac{\partial \mathbf{D}}{\partial s} + \underbrace{\frac{\partial \mathbf{R}}{\partial \lambda}}_{\mathbf{F}_0} \frac{\partial \lambda}{\partial s} = \mathbf{0}. \tag{7}$$

Multiplying Eq. (7) from the left by the transpose of the eigenvector $\boldsymbol{\Phi}^\mathrm{T}$, which corresponds to the zero eigenvalue $\kappa = 0$, results in

$$\boldsymbol{\Phi}^\mathrm{T} \mathbf{K}_\mathrm{T} \frac{\partial \mathbf{D}}{\partial s} + \boldsymbol{\Phi}^\mathrm{T} \mathbf{F}_0 \frac{\partial \lambda}{\partial s} = \mathbf{0}. \tag{8}$$

At a critical point, that is $\boldsymbol{\Phi}^\mathrm{T}\mathbf{K}_\mathrm{T} = \mathbf{0}$, as shown in Eq. (5), the left term of Eq. (8) vanishes. To satisfy Eq. (8), either $\boldsymbol{\Phi}^\mathrm{T}\mathbf{F}_0$ or $\frac{\partial \lambda}{\partial s}$ has to vanish. In the latter case of vanishing $\frac{\partial \lambda}{\partial s}$, the critical point is a limit point. The other case, that is $\boldsymbol{\Phi}^\mathrm{T}\mathbf{F}_0 = 0$, indicates a bifurcation point. This means that, if the buckling vector (the critical mode shape) is orthogonal to the external load, buckling occurs. The characteristics of critical points can be summarized as:

$$|\mathbf{K}_\mathrm{T}| = 0 \rightarrow \text{critical point} \quad \begin{cases} \boldsymbol{\Phi}^\mathrm{T}\mathbf{F}_0 = 0 \rightarrow \text{bifurcation point (B)} \\ \boldsymbol{\Phi}^\mathrm{T}\mathbf{F}_0 \neq 0 \rightarrow \text{limit point (L)} \end{cases} \tag{9}$$

### 2.3. Stability analysis

In geometrically nonlinear problems, detection of critical points is usually performed by tracing equilibrium paths in an incremental iterative manner. Corresponding path following or continuation methods have been described in numerous contributions, see for instance [20–24], among many others. Depending on the characteristics of nonlinear equilibrium paths, several different path following schemes can be utilized to trace it. Path following methods mainly differ in the controlled quantity and the corresponding constraint equation. Load control, displacement control (see for instance [21] or [25]) and arc-length control (see for instance [22–24]) are important particular cases. While an arc-length procedure may be capable of tracing any arbitrary path, other methods fail at certain points. At a limit point, load controlled methods fail due to the fact that the load cannot be further increased. Post-critical behavior cannot be examined in this way. Displacement controlled methods fail if the controlled displacement cannot be increased locally. This phenomenon occurs if the equilibrium path has a vertical tangent ("snap-back"). The previously mentioned contribution in the context of IGA by Guo et al. [17] utilizes the arc-length method for the solution of nonlinear stability problems. Leonetti et al. [16] deal with Koiter's theory for buckling and initial post-buckling analysis. There also exist methods for direct computation of critical points, also known as extended systems, see for instance [26], [27] and [28].

In the present contribution, the above mentioned concepts are not considered in more detail, since some types of stability problems allow for simplified solution strategies. So-called pre-buckling analyses (PBA) may be utilized to approximately identify critical points. By solving a generalized linear eigenvalue problem, the load factor and the corresponding buckling modes can be predicted in a straightforward manner. The governing equations for the different types of PBA are derived in the following.

First, we recall that the tangent stiffness matrix $\mathbf{K}_\mathrm{T}$ can be decomposed into three parts,

$$\mathbf{K}_\mathrm{T} = \mathbf{K}_\mathrm{e} + \overbrace{\mathbf{K}_\mathrm{u} + \mathbf{K}_\mathrm{g}}^{\text{nonlinear}}. \tag{10}$$

$\mathbf{K}_\mathrm{e}$ is the linear *elastic stiffness matrix*, $\mathbf{K}_\mathrm{u}$ denotes the *initial displacement stiffness matrix* (resulting from changing geometry due to deformation) and $\mathbf{K}_\mathrm{g}$ is the *initial stress stiffness matrix* or *geometric stiffness matrix*. The sum of $\mathbf{K}_\mathrm{e}$ and $\mathbf{K}_\mathrm{u}$ is usually denoted as *material part* of the stiffness matrix.

The key assumption is that the nonlinear parts of $\mathbf{K}_\mathrm{T}$ depend approximately linearly on the load, represented by the load factor $\lambda$. Formally, this can be expressed as a truncated series expansion of the stiffness matrix as

$$\mathbf{K}_\mathrm{T} = \mathbf{K}_\mathrm{T}|_{\lambda=0} + \frac{\partial \mathbf{K}_\mathrm{T}}{\partial \lambda}\lambda + \text{H.O.T.}, \tag{11}$$

with

$$\frac{\partial \mathbf{K}_{\mathrm{T}}}{\partial \lambda} = \frac{\partial \mathbf{K}_{\mathrm{u}}}{\partial \lambda} + \frac{\partial \mathbf{K}_{\mathrm{g}}}{\partial \lambda} =: \mathbf{K}_{\mathrm{u}}^{\mathrm{LIN}} + \mathbf{K}_{\mathrm{g}}^{\mathrm{LIN}}, \tag{12}$$

where the superscript "LIN" indicates linearized quantities. The condition for critical points (5) then gives rise to the generalized eigenvalue problem

$$\left(\mathbf{K}_{\mathrm{e}} + \lambda \left(\mathbf{K}_{\mathrm{u}}^{\mathrm{LIN}} + \mathbf{K}_{\mathrm{g}}^{\mathrm{LIN}}\right)\right) \boldsymbol{\Phi} = \mathbf{0}. \tag{13}$$

The accuracy of the results obtained from pre-buckling analysis depends on how well the assumption of the stiffness depending linearly on the load is satisfied. It is mostly very good, if the equilibrium path up to the first critical point (the *pre-buckling path*) is approximately linear. This is often the case for bifurcation points, but rarely for limit points. Neglecting the initial displacement matrix, Eq. (13) reduces to

$$\left(\mathbf{K}_{\mathrm{e}} + \lambda \mathbf{K}_{\mathrm{g}}^{\mathrm{LIN}}\right) \boldsymbol{\Phi} = \mathbf{0}. \tag{14}$$

In the literature, (14) is often denoted as *classical pre-buckling analysis* whereas Eq. (13) is referred to as *linear pre-buckling analysis*. For systems with zero deflection prior to buckling both equations yield identical results. Indeed, for the systems considered in this study, the displacements at the critical points are very small such that the effect from $\mathbf{K}_{\mathrm{u}}^{\mathrm{LIN}}$ is negligible compared to the one from $\mathbf{K}_{\mathrm{g}}^{\mathrm{LIN}}$. In this case, both types of pre-buckling analyses yield practically the same results. This is typical for bifurcation problems, as opposed to snap-through problems.

The linearized geometric stiffness of one finite element $e$ can be computed as

$$\mathbf{k}_{\mathrm{g},e}^{\mathrm{LIN}} = \int_{\Omega_e} \frac{\partial^2 \mathbf{E}}{\partial \mathbf{d} \partial \mathbf{d}} : \mathbf{S}^{\mathrm{LIN}} \mathrm{d}\Omega, \tag{15}$$

where $\Omega_e$ is the domain occupied by the element and $\mathbf{d}$ is the vector of degrees of freedom on element level. The second derivative of the Green–Lagrange strain with respect to the nodal degrees of freedom $\frac{\partial^2 \mathbf{E}}{\partial \mathbf{d} \partial \mathbf{d}}$ is constant (independent of the displacements) and can be computed analytically. $\mathbf{S}^{\mathrm{LIN}}$ is the linearized second Piola–Kirchhoff stress tensor, computed from the linearized Green Lagrange strain tensor $\mathbf{E}^{\mathrm{LIN}}$ via the material law. Technically, it is obtained from a linear static analysis with $\lambda = 1$, see Wriggers [29]. Assembly of $\mathbf{k}_{\mathrm{g},e}^{\mathrm{LIN}}$ to the system matrix $\mathbf{K}_{\mathrm{g}}^{\mathrm{LIN}}$ follows the standard procedure.

An approximation of $\mathbf{K}_{\mathrm{u}}^{\mathrm{LIN}} + \mathbf{K}_{\mathrm{g}}^{\mathrm{LIN}}$ can be obtained numerically from a forward difference step by performing a linear analysis with a very small load factor $\lambda_\varepsilon$,

$$\mathbf{K}_{\mathrm{e}} \mathbf{D}_\varepsilon = \lambda_\varepsilon \mathbf{F}_0 \quad \rightarrow \quad \mathbf{D}_\varepsilon, \tag{16}$$

computing the tangent stiffness $\mathbf{K}_{\mathrm{T}}(\mathbf{D}_\varepsilon)$ and subtracting the elastic stiffness matrix provides an approximation of the linearization as

$$\mathbf{K}_{\mathrm{u}}^{\mathrm{LIN}} + \mathbf{K}_{\mathrm{g}}^{\mathrm{LIN}} \approx \frac{1}{\lambda_\varepsilon} \left(\mathbf{K}_{\mathrm{T}}(\mathbf{D}_\varepsilon) - \mathbf{K}_{\mathrm{e}}\right). \tag{17}$$

This is how the linearized stiffness matrices have been obtained for the numerical computations in the case study in Section 3. It has been checked that the results are identical for the reported number of digits to the results obtained with a classical prebuckling analysis using the exact linearization from Eq. (15). This means that indeed the contribution from $\mathbf{K}_{\mathrm{u}}^{\mathrm{LIN}}$ is negligible and the numerical derivative is accurate enough.

The lowest eigenvalue of Eq. (13) or Eq. (14), respectively, provides an approximation of the critical load factor $\lambda_{\mathrm{crit}}$. Multiplying $\lambda_{\mathrm{crit}}$ with the initial load $\mathbf{F}_0$ yields the critical load $\mathbf{F}_{\mathrm{crit}}$, that is the *buckling load*. The corresponding eigenvector $\boldsymbol{\Phi}_{\mathrm{crit}}$ represents the critical buckling mode shape.

In most cases, the matrices $\mathbf{K}_{\mathrm{u}}^{\mathrm{LIN}}$ and $\mathbf{K}_{\mathrm{g}}^{\mathrm{LIN}}$ are not positive definite, which may be challenging for numerical algorithms. Thus, shifting techniques are required to solve the eigenvalue problems shown in Eqs. (13) and (14).

## 3. Case studies

### 3.1. Objective and analysis method

A frequently mentioned key feature of IGA is the use of "exact" geometry from CAD for computation. Besides possible savings in time due to simplified workflows and avoidance of (re-)meshing, a key question is, whether

more accurate results can be achieved through more accurate geometry. The aim of this section is to identify the influence of exact geometry representation in pre-buckling analyses of shells. The presented set of case studies aims to systematically separate the effects of *geometry approximation* from effects of *solution approximation*. Solutions obtained by isogeometric shell elements are compared with standard shell finite element solutions obtained with the commercial software ANSYS 18.0.

In all case studies, loads are applied in the form of prescribed displacements along boundaries of the structure, because this is the type of load typically applied in laboratory experiments. In this context, the load factor $\lambda$ drives the magnitude of the prescribed displacements instead of the related forces. The corresponding boundary value problems can be reformulated to match the format of a standard load case with prescribed forces. Essentially, the vector of external forces represents the support reactions in the mechanism that applies the prescribed displacements. It still depends on $\lambda$, but it is not necessarily linear in $\lambda$. However, the notion of a critical load factor $\lambda_{\text{crit}}$ directly transfers to this scenario and the methods for PBA described in the previous section are readily applicable. Moreover, for the problems studied here, the characteristics of the pre-buckling path are such that the external forces are practically proportional to $\lambda$.

### 3.2. Overview of structural models, discretization schemes and solution procedures

For the sake of comprehensibility, we give a detailed description of the employed element formulations and solution procedures. Isogeometric analysis (IGA) proposed by Hughes et al. [10] is employed using NURBS (Non-Uniform Rational B-Splines). We utilize the so-called $k$-refinement strategy for obtaining quadratic, cubic and quartic discretizations with maximum $C^{p-1}$-continuity within each patch. Various different isogeometric shell formulations could possibly be employed. However, for the static linear thin shell stability problems studied here, the discrepancy between different shell models is small. In the context of material and geometrical nonlinearities, as well as for dynamic problems, different isogeometric shell formulations suggest themselves for a comparative study, also including the influence of locking. This, however, is out of the scope of the present paper.

Instead, we focus on one single isogeometric shell formulation, namely:

- IGA KL: an isogeometric Kirchhoff–Love (KL) shell formulation with numerical integration through the shell's thickness, as presented in [30], which should provide, for the chosen problem setups, practically identical results as the isogeometric KL shell formulation from [2]. All discretizations contain at least quadratic, $C^1$-continuous NURBS shape functions within a patch. Multi-patch geometries are coupled via the bending strip method from [31]. In the shell's in-plane directions, we use a "full" integration scheme with $p+1$ Gauss points, where $p$ is the polynomial degree of the shape functions. Two integration points in thickness direction are used.

All isogeometric shell analyses are performed in NumPro, the C++ based, object oriented in-house finite element program of the Institute for Structural Mechanics at the University of Stuttgart. Linear buckling analyses according to Eq. (13) are performed, where the sum of the linearized geometric and initial displacement stiffness is computed numerically according to Eq. (17). The generalized eigenvalue problem, Eq. (13), is solved by the package Arpack++ [32,33]. The package offers a huge number of procedures to solve several types of large scale eigenvalue problems based on the "Implicitly Restarted Arnoldi Method" [34]. Particularly, we use the class for symmetric generalized eigenvalue problems referred to as "ARluSymGenEig" in combination with the "buckling mode". This mode employs a shifting technique to determine eigenvalues near a user defined shift value. Using this combination of "class" and "mode" to solve a problem of the form $(\mathbf{A}-\lambda\mathbf{B})\boldsymbol{\Phi}=\mathbf{0}$, the Matrix $\mathbf{A}$ is required to be positive semi-definite, whereas no further requirements for $\mathbf{B}$ apply. Thus, the algorithm is capable of handling non-positive definite or semi-definite matrices $\mathbf{B}$.

The results obtained by IGA KL are compared with results obtained with the commercial finite element analysis software ANSYS 18.0. Four different types of elements from ANSYS are used:

- SHELL63: a 4-node quadrilateral element of KL type, bi-linear Lagrange polynomials as shape functions for the membrane part and a patch of 4 Discrete Kirchhoff Triangles (see [35–38]) for the bending part.

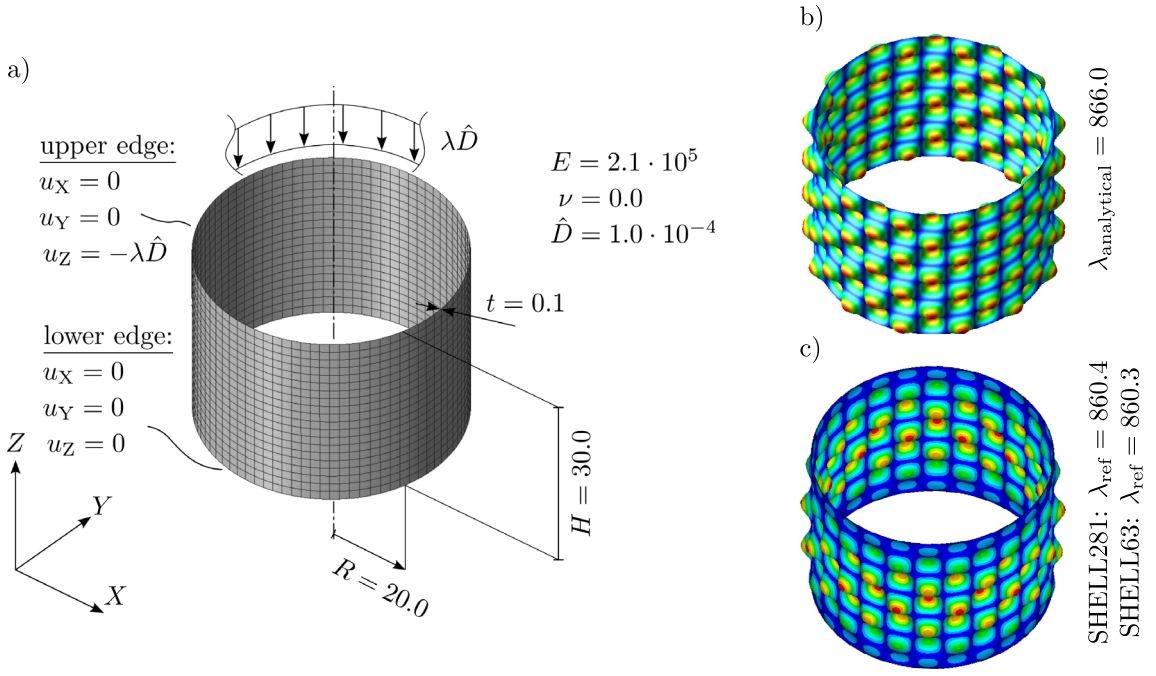


**Fig. 2.** Exact cylinder subjected to axial compression (Dirichlet-type load): (a) problem setup, (b) analytical solution, (c) reference solution.

- SHELL181R: a 4-node quadrilateral element of Reissner–Mindlin (RM) type, reduced integration with hourglass control to remove locking effects.
- SHELL181F: a 4-node quadrilateral element of RM type, full integration, incompatible modes and Assumed Natural Strains to avoid locking, see [39,40].
- SHELL281: an 8-node quadrilateral serendipity element of RM type, quadratic shape functions, reduced integration with $2x2$ in-plane integration points.

Each finite element formulation uses three translational and three rotational degrees of freedom per node. SHELL281 uses quadratic shape functions and eight nodes per element. Thus, the initial geometry of curved structures can be approximated more accurately than for the other elements. It is worth mentioning that the ANSYS documentation [41] suggests the use of SHELL181 instead of SHELL63. Pre-buckling analysis in ANSYS requires a linear static analysis as a first step. Based on the results of the linear analysis, the linearized geometric stiffness matrix is computed. The subsequent buckling analysis uses the Block Lanczos algorithm. An automated shift strategy with a user defined initial shift is employed. Especially for large problems the computation can be accelerated significantly by choosing an initial shift close to the lowest eigenvalue. To our best knowledge ANSYS uses classical pre-buckling analysis given by Eq. (14).

### *3.3. Cylindrical shell subject to axial compression*

The first case study deals with stability analyses of a cylindrical shell subjected to axial compression, as shown in Fig. 2(a) with all dimensions and material properties. With a slenderness ratio of $\frac{R}{t} = \frac{20}{0.1} = 200$ the shell can be classified as a thin shell $\left(\frac{R}{t} \geq 20\right)$. Transverse shear strains may be neglected and KL type shell theory may be used, since the expected differences of results obtained by KL and RM type shell elements are negligible.

A linear elastic material is assumed with Poisson's ratio $\nu = 0.0$ in order to avoid boundary layer effects that could obstruct the view on the effects under investigation. The axial compression is applied using a displacement boundary condition in order to enforce the upper edge to remain a planar circle. The upper edge is fixed in horizontal

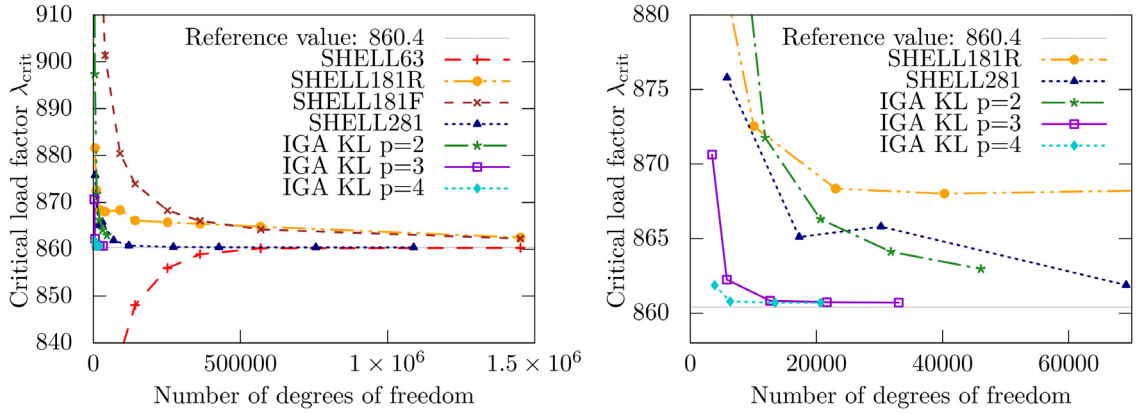


**Fig. 3.** Axially compressed cylinder: convergence of the critical load factor over the number of DOF; left: whole range; right: zoom.

directions, the lower edge of the cylindrical shell is fixed in all three directions. All defined boundary conditions are also shown in Fig. 2(a). For this type of loading, a regular checkerboard buckling pattern is expected.

The NURBS-based discretization consists of four coupled patches, representing the exact geometry of a cylinder. In the classical finite element approach using the commercial software ANSYS, the cylindrical shell is discretized using the shell elements summarized in Section 3.2. Cylindrical surfaces are ruled surfaces. However, using linear or quadratic polynomials as shape functions, it is not possible to obtain a discretization with exact geometry representation. For the same element size, the quadratic shell element SHELL281 provides a better approximation of the geometry than the linear elements SHELL181 and SHELL63. For increasing levels of mesh refinement, decreasing geometry errors are achieved.

Both an analytical reference solution and numerical reference solutions are used for comparison. The first numerical "overkill" solution is obtained using SHELL281 and a fine mesh with about $1.1 \cdot 10^6$ DOF. The resulting critical load factor $\lambda_{ref} = 860.4$ and the corresponding mode shape are shown in Fig. 2(c). The second numerical reference solution is computed using SHELL63 and a mesh with about $1.5 \cdot 10^6$ DOF. There is no difference in the critical mode shape and only a slight difference in the critical load factor, which is about 860.3 for SHELL63. The shape of the converged critical buckling mode shows 7 half waves in axial direction and 26 half waves or rather 13 full waves in hoop direction. An analytical verification is carried out using [42], which yields for this mode shape a corresponding critical load factor of 866.0, as shown in Fig. 2(b). A small discrepancy between the analytical solution and the experimental solution for the buckling load factors is observed. This deviation stems from buckles fading out at both ends of the cylinder in the numerical solution, which is not captured by the analytical solution, assuming a strictly periodic buckling pattern by construction.

Fig. 3 (left) shows the convergence of the critical load factor with respect to the number of DOF for the whole range of investigated meshes. A zoom into the coarse mesh range is shown in Fig. 3 (right). Both figures show significant differences in the approximation quality for the compared elements. Although computational effort is of course not proportional to the number of degrees of freedom, some general conclusions can be drawn from this diagram. First, as expected, higher order discretization schemes converge more quickly than lower order ones. It is partly for this reason, that the results from the NURBS-based discretizations (IGA) are apparently superior to the ones obtained with standard finite element discretizations. Especially the approximations using the bilinear SHELL181 element and the SHELL63 element converge very slowly. However, both quadratic elements, that is SHELL281 and IGA KL p=2, yield a comparable convergence behavior of the critical load factor.

In order to further study the difference in performance of the applied element formulations, we will now focus on the buckling mode shapes. Fig. 4 shows the evolution of critical mode shapes, that is the eigenvectors associated with the smallest eigenvalues, of all employed element types. For the standard finite element discretizations, very fine meshes are needed to obtain the correct buckling mode shapes. Wrong modes are obtained even if the critical load factors are already practically converged. For instance, a discretization with 362880 DOF using SHELL63 yields a

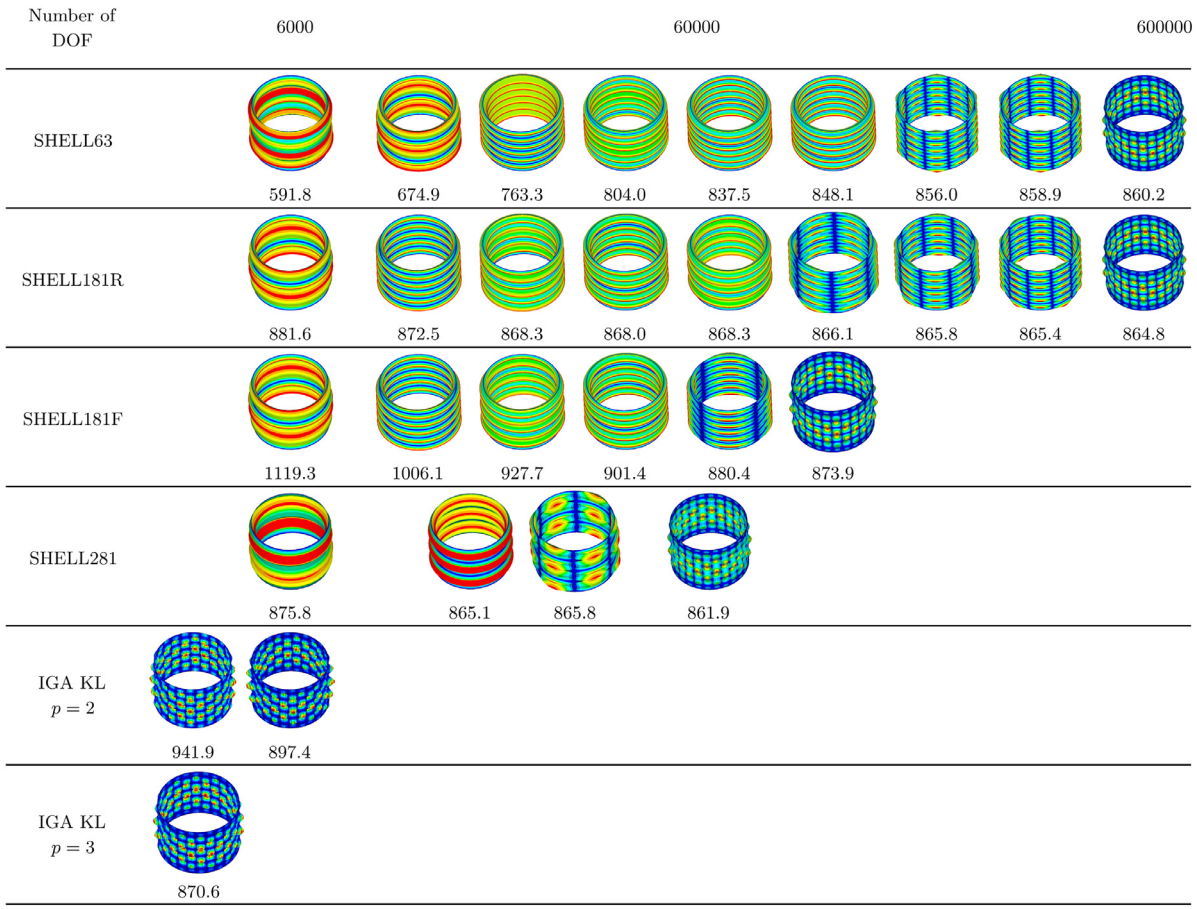


**Fig. 4.** Axially compressed cylinder: critical mode shapes and corresponding critical load factors for different discretizations: evolution of the mode shapes. The plots of the buckling modes are positioned approximately according to the logarithmic scale of the number of DOF.

critical load factor of about 860, which is almost identical to the numerical reference solution, but a wrong buckling mode. To represent the correct mode shape using SHELL63 or SHELL181R – the default version of SHELL181 in ANSYS – more than 500000 DOF are needed. Using the IGA KL element with $p = 3$, only about 3500 DOF are necessary to predict the correct mode shape, although the critical load factor is not yet fully converged. This is less than 1% of the total of DOF compared to SHELL63 and SHELL181R. Comparing the necessary DOF for IGA KL $p = 3$ and SHELL181F, the fraction is about 2.5%. Compared to the quadratic shell element SHELL281, the IGA KL $p = 2$ discretization requires 7.6% of DOF and the IGA KL $p = 3$ discretization requires 5% of DOF to predict to correct buckling mode.

Although these numbers appear to be impressive, conclusions have to be drawn with care, as the formulations differ in various aspects. For instance, the geometric stiffness matrices of KL and RM type elements have different properties, which may have an influence on the numerical properties of the eigenvalue problem. Moreover, a typical property of shell buckling problems is that there exist several critical points with almost identical critical load factors, that is eigenvalues. Fig. 5 shows the five lowest eigenvalues and the 31st eigenvalue together with the corresponding buckling modes, obtained with the first numerical reference solution using SHELL281. The first five eigenvalues take on values between 860.4 and 862.2, which is a range of about 0.2%. The 31st eigenmode is shown because it is similar to buckling modes that are found to be critical in several “coarse” mesh discretizations, as shown in Fig. 4. With increasing refinement, it is likely that a change in order of the eigenmodes comes along with only a small change of the eigenvalue. For instance, the critical mode shapes using SHELL181 and a discretization with

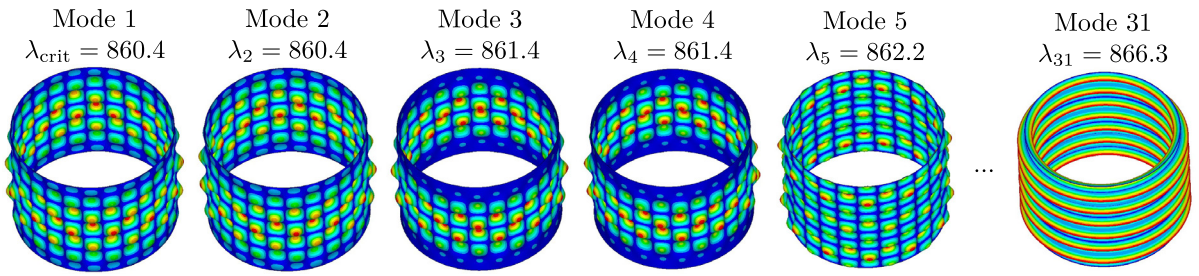


**Fig. 5.** Axially compressed cylinder: smallest five eigenvalues and 31st eigenvalue with corresponding mode shapes; numerical reference solution obtained with SHELL281.

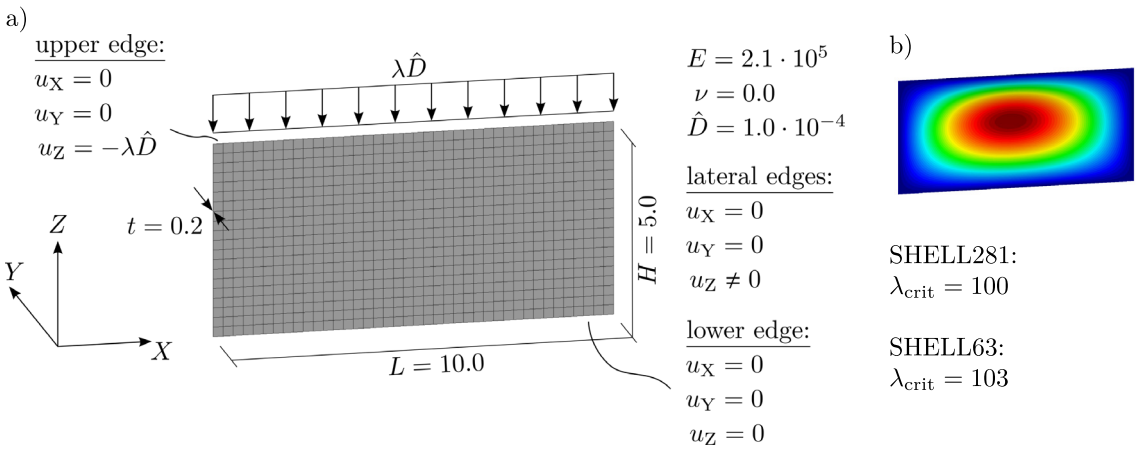


**Fig. 6.** Flat plate subjected to compression (Dirichlet-type load): (a) problem setup, (b) reference solution.

10080 DOF yield this shape. The corresponding 31st eigenvalue is 866.3, which deviates only about 0.7% from the reference value 860.4. This mode is only chosen exemplarily, other modes could be chosen and identified in Fig. 4.

Obviously, the change of the order within the eigenmodes plays a decisive role for these results. The question naturally arises, whether in the coarser discretizations that provided the wrong buckling mode as the critical one, the correct mode appears later, for instance along with the 2nd or 3rd (or any low count) eigenvalue. We therefore exemplarily checked higher order mode shapes but found this hypothesis to be falsified. In some cases, the finest discretization that did *not* yet provide the correct mode as the first one, the correct mode appeared as higher order mode. For instance, the correct mode was found corresponding to the 13th eigenvalue for the solution obtained by SHELL181R with 362880 DOF.

In the light of the results from this first case study, it is of paramount interest, to investigate the sources of the superior accuracy of solutions obtained by IGA. In particular, the question arises, whether exact geometry representation is the driving force for superior accuracy.

### *3.4. Buckling of a flat panel*

The aim of this and the following case study is to separate the effect of exact geometry representation from the effects resulting from higher order and smoothness of the shape functions, that is the approximation power of NURBS. Therefore, geometries are investigated that can be exactly represented by all investigated element formulations.

This is trivially possible for the simply supported flat plate shown in Fig. 6(a). The two lateral edges are free along the $Z$-direction and fixed in transverse directions $X$ and $Y$. The upper edge is fixed in $X$- and $Y$-directions and the load is applied using an inhomogeneous Dirichlet boundary condition in $Z$-direction, while the lower edge

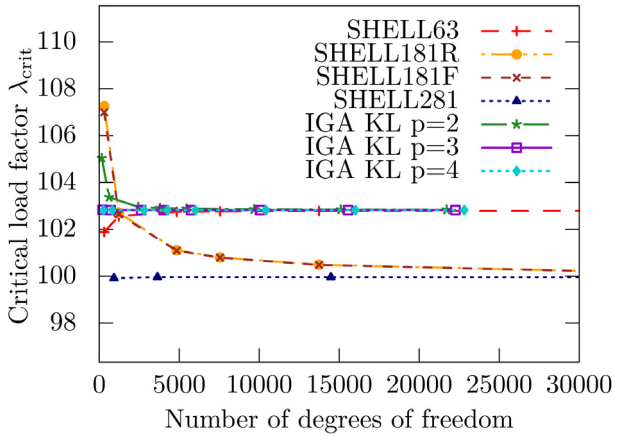


**Fig. 7.** Flat plate: convergence of the critical load factor (corresponding mode shape from reference solution shown right) over the number of DOF.

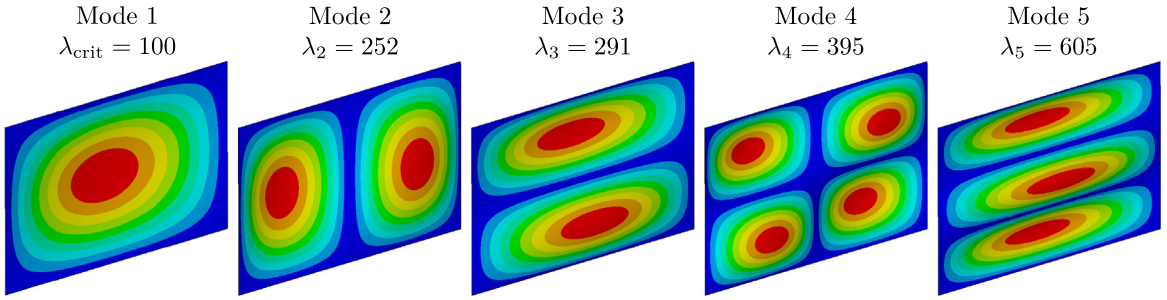


**Fig. 8.** Flat plate: five smallest eigenvalues and corresponding mode shapes.

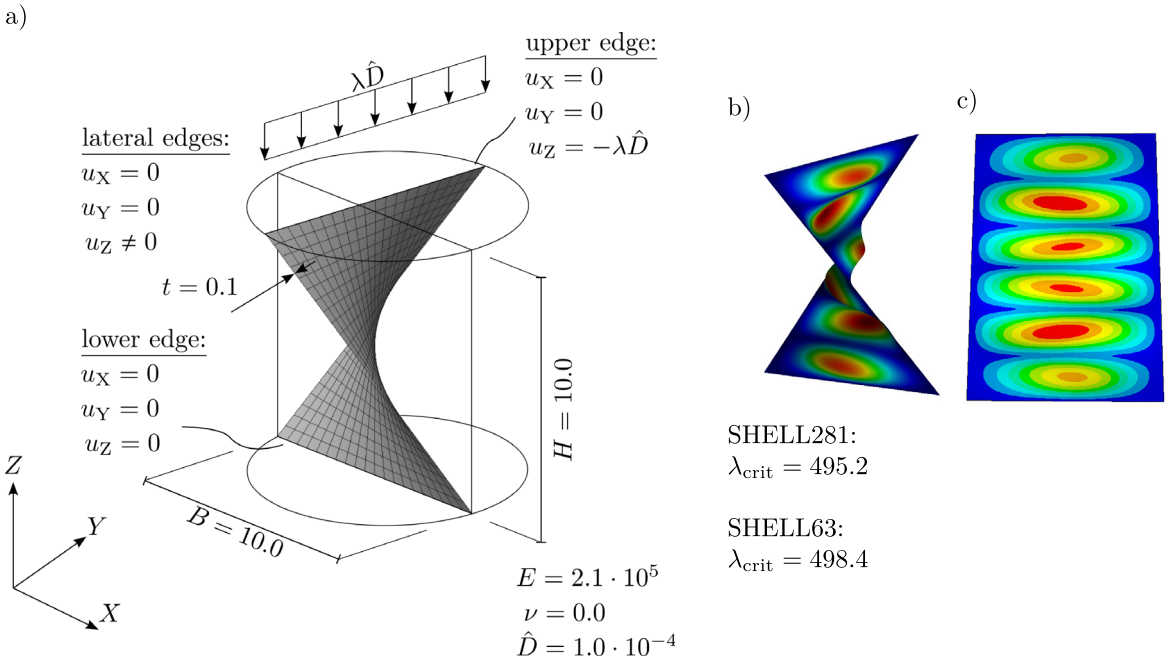


**Fig. 9.** Hyperbolic paraboloid subjected to compression (Dirichlet-type load): (a) problem setup, (b) reference solution in side view, (c) reference solution in front view.

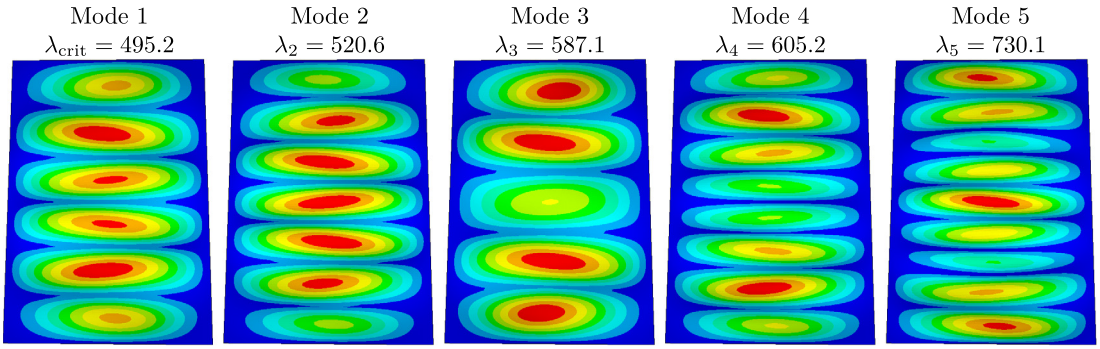


**Fig. 10.** Hyperbolic paraboloid: five smallest eigenvalues and corresponding mode shapes.

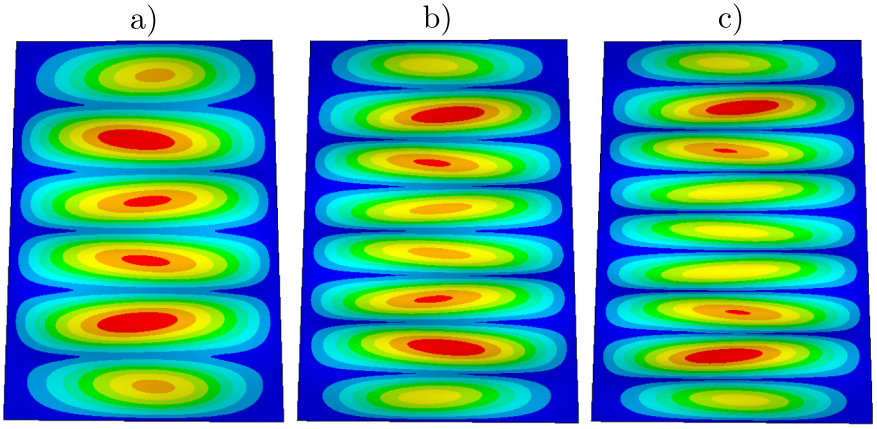


**Fig. 11.** Hyperbolic paraboloid: critical mode shapes for slendernesses (a) 100, (b) 200 and (c) 300.

is fixed in all three directions. Also in this case, numerical reference solutions are computed using SHELL281 and SHELL63 with fine meshes. The resulting mode shape and the corresponding converged critical load factors are shown in Fig. 6(b).

Convergence of the critical load factor with respect to the number of DOF is shown in Fig. 7. The results of the KL type shell elements slightly differ from the ones obtained with RM elements. With a slenderness of $\frac{H}{t} = \frac{5}{0.2} = 25$, transverse shear effects play a more pronounced role than for the previous problem setup of the cylinder (slenderness $\frac{R}{t} = 200$).

In contrast to the cylindrical shell problem, computation of the buckling modes yields correct results for all elements and discretizations already for the coarsest meshes. Apparently, the problem is too simple. Fig. 8 shows the five smallest eigenvalues for the reference solution and the corresponding mode shapes. The results are shown for a simulation using SHELL281 with a mesh of $200 \times 100$ elements and $3.6 \cdot 10^5$ DOF. It can be seen that the eigenvalues differ significantly, such that a change of order of these clearly separated eigenmodes is very unlikely. Therefore, a more demanding problem setup is studied next.

### *3.5. Hyperbolic paraboloid*

Based on the hypothesis that curved geometries provide potentially more demanding setups than flat ones, a shell with the shape of a hyperbolic paraboloid, as shown in Fig. 9, is considered next. This particular geometry is chosen, because it can be exactly represented by bilinear finite elements. All boundary conditions are similar to those applied to the flat panel and are given in detail in Fig. 9.

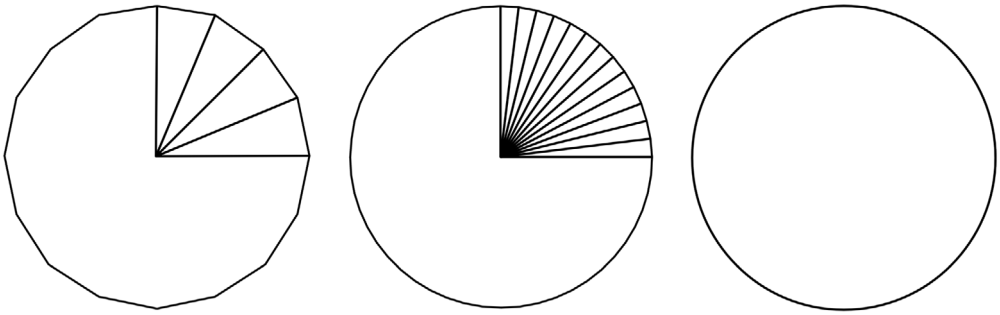

**Fig. 12.** Segmented cylinder: Approximation of circle, left: 16 segments, center: 52 segments, right: perfect circle.

However, also in this case, there is no significant difference in the results obtained using standard finite elements and NURBS-based discretizations (convergence curves are omitted for the sake of brevity). Fig. 10 shows the first five eigenvalues and eigenmodes for a discretization using SHELL281 with a mesh of 100 $\times$ 123 elements and $2.2 \cdot 10^5$ DOF. When considering the number of buckles, the order of the resulting eigenmodes seems counter intuitive. Therefore, these results have been verified and confirmed by further mesh refinement. The background of this phenomenon deserves further attention, but it is not investigated in this study, as it is only remotely related to the scope of the present work, dealing with the more abstract topic of approximation power of discretization schemes. The eigenvalues are indeed closer to each other than in the case of the flat panel, but still clearly separated such that a change of order is not likely. Also the variation of the thickness and thus the slenderness did not yield qualitatively different results. As shown in Fig. 11, the number of half-waves slightly increases with increasing slenderness, but the complexity of the buckling pattern is not as pronounced as it is for the patterns observed in Section 3.3 for the cylindrical shell problem. In summary, the studies with simple "exact geometries" in this and the previous section remain inconclusive concerning the question towards significance of exact geometry.

### *3.6. Segmented cylinder*

The idea of this last case study is to maintain the complexity of the cylindrical shell problem studied in Section 3.3, while introducing intentional geometry errors, which are identical for all element types, discretization schemes and levels of mesh refinement. This is accomplished by solving the problem of a segmented cylinder, as described in the following. Fig. 12 exemplarily shows the plan view of three different segmentations of a circle, building the base for the cylinder. An overview of the deviation of the segmented cylinder for the investigated segmentations in comparison to the perfect cylinder with a circle as basis is shown in Table 1. The numbers of segments are not randomly chosen. As we expect 26 half-waves in hoop direction, the segmentations with 26 and 52 represent attractive "offers" for obtaining the correct solution. The number of segments is then further increased up to 120. The key idea of this case study is to keep the approximation error in the geometry – assuming the perfect cylinder as reference – constant, while the number of DOF is increased by mesh refinement within each flat segment. In the first part of this section, the segmented cylinder problem is investigated with the standard finite element approach using ANSYS. In the second part, the problem is studied by IGA.

#### *Standard finite element solution*

As already described in Section 3.2, four different types of shell elements are used for the finite element solutions in ANSYS. In contrast to Section 3.3, the geometry error is independent of the mesh. All other aspects of the problem setup are identical to the cylindrical shell problem, as shown in Fig. 2. The cylinder with a radius of R = 20.0, height H = 30.0 and thickness t = 0.1 is again subjected to a vertical displacement of $\hat{D} = 1.0 \cdot 10^{-4}$ on the upper edge by an inhomogeneous Dirichlet boundary condition. The lower edge of the cylinder is fixed in all three directions and Poisson's ratio is zero.

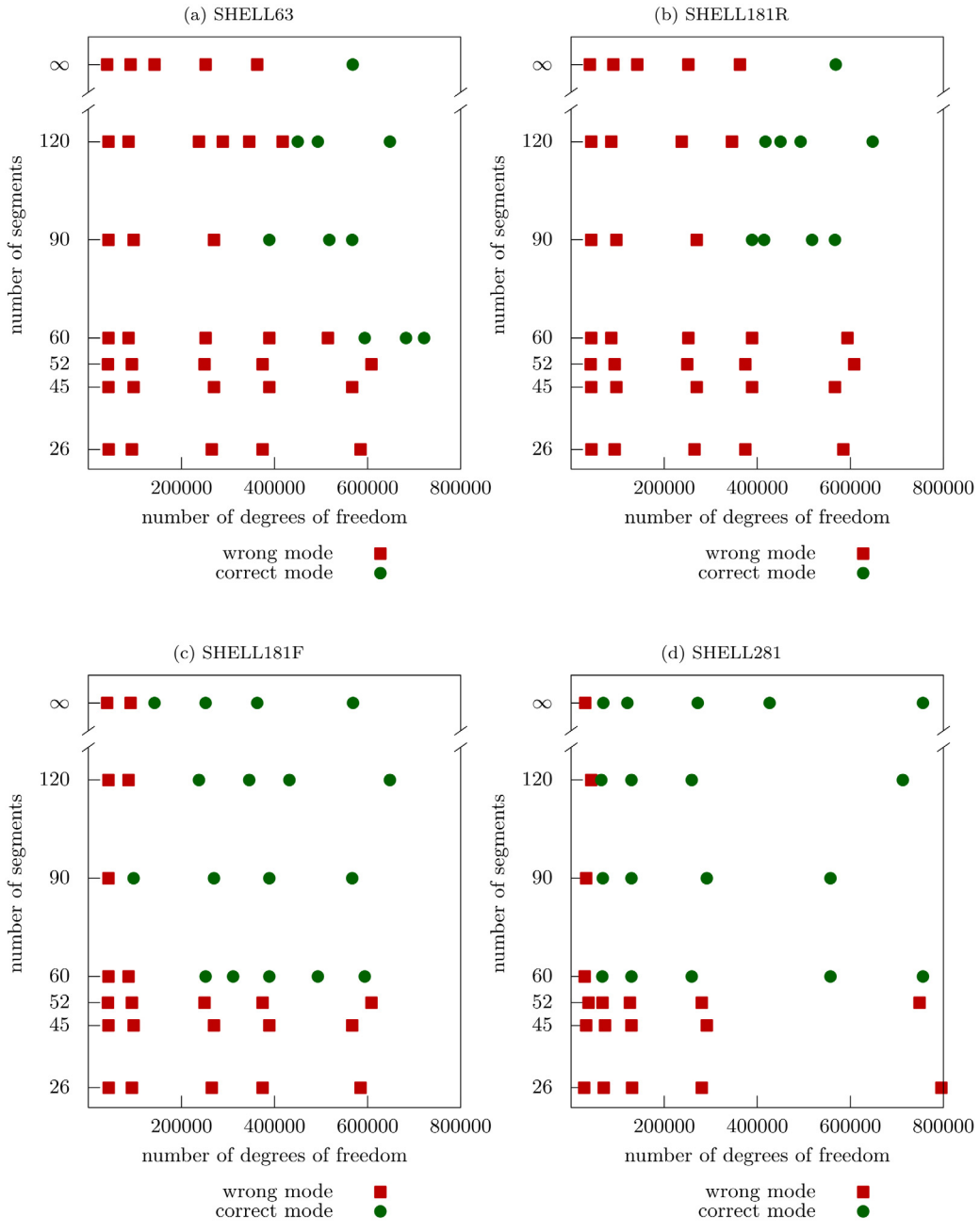


**Fig. 13.** Segmented cylinder: Occurrence of the correct buckling mode for the four different ANSYS elements. Number of segments for the geometry approximation over number of DOF. Green dots indicate the correct buckling mode, red squares indicate a wrong buckling mode.

**Table 1**
Deviation segmented cylinder — perfect cylinder.

| Number of segments | 26 | 45 | 52 | 60 | 90 | 120 |
|---|---|---|---|---|---|---|
| deviation of lateral surface in % | 0.24 | 0.08 | 0.06 | 0.05 | 0.02 | 0.01 |
| deviation of base area in % | 0.97 | 0.32 | 0.24 | 0.18 | 0.08 | 0.05 |

In this case study, we are primarily interested in the evolution of the predicted buckling mode. Convergence studies of the critical load factor have been performed as well, but they are not reported here, as they do not provide additional insight. The diagrams in Fig. 13 summarize the results for the buckling modes obtained by simulations with the four different types of shell elements from ANSYS. The occurrence of correct or wrong critical buckling modes is shown in dependence of the number of segments and the number of DOF. Here, buckling modes of the segmented shell are considered "correct", if the number of halfwaves in hoop direction and the number of halfwaves in axial direction comply with the reference solution for the perfect cylinder. Of course, for an actual segmented shell, different modes may be correct, but the scenario here is to interpret the segmentation as a geometry approximation error, while aiming to solve the (perfect) cylindrical shell problem. In each of the four diagrams, red squares represent wrong buckling mode shapes and green dots represent correct buckling modes. In the appendix, the data for each number of segments, the corresponding number of DOF, the critical load factor $\lambda_{\text{crit}}$ and whether the correct buckling mode occurred is shown in the form of multiple tables for the different ANSYS and IGA KL elements. The results for the perfect cylindrical geometry, already shown in Fig. 4, are repeated in the top line of each diagram, with the label $\infty$ indicating an infinite number of segments. In all cases, except for SHELL181R, an approximation of the cylindrical geometry with 60 segments is sufficient to obtain the correct buckling mode. For coarser segmentations, different (wrong) buckling modes are obtained, even for very fine meshes. This observation indicates some threshold in geometry approximation, beyond which the geometry error is small enough to allow convergence to the correct result.

For the KL type element SHELL63, more than 400000 degrees of freedom are necessary to obtain the correct mode. For the RM type element SHELL281 some 80000 DOF are sufficient. The most interesting fact is, however, that, independent of the element type, for finer segmentations the number of DOF needed to obtain the correct mode does *not* decrease. This suggests the conclusion that better geometry approximation does *not* result in an improved coarse mesh accuracy in view of the quality of the predicted buckling mode.

*IGA solution*

In the context of IGA, each segment is represented by one patch. Patch coupling is performed via the bending strip method [31]. Since for the standard finite element approach the first correct results show up for 60 segments, we use this particular geometry approximation for further investigations. Fig. 14 summarizes the results for the buckling modes using IGA KL elements in dependence of the polynomial degree $p$ and the number of DOF. As before, correct buckling modes are represented by green dots, whereas red squares indicate wrong buckling modes. Correct buckling modes are achieved in all cases in the range between 10000 and 20000 DOF. It may appear counter-intuitive that the number of DOF needed to obtain the correct buckling mode increases with the polynomial order. The reason is the fact that the $C^0$-continuous edges in the segmented shell artificially increase the number of DOF for higher order discretizations via knot repetition.

Qualitatively, however, the same results are achieved by IGA KL as for the exact cylinder problem. This underlines that an exact representation of the geometry is not needed for these problem types and the superior results of IGA are based on the high approximation power of smooth NURBS.

## 4. Summary and outlook

In this paper, we presented a comprehensive study on the approximation power of NURBS in the context of isogeometric analysis and the significance of exact geometry in linear pre-buckling analyses of shells. Numerous different finite element solutions obtained with the commercial software ANSYS were compared with solutions obtained by isogeometric shell analysis. We observed superior accuracy of isogeometric shell analyses compared to standard finite element analyses, particularly in detecting buckling modes.

One result is, that for the studied class of problems isogeometric shell formulations require only a fractional amount of degrees of freedom for the same level of accuracy compared to standard finite elements. This effect seems to be particularly pronounced if numerous critical points appear within a small range of load levels. This is, for instance, the case for buckling of axially compressed cylinders.

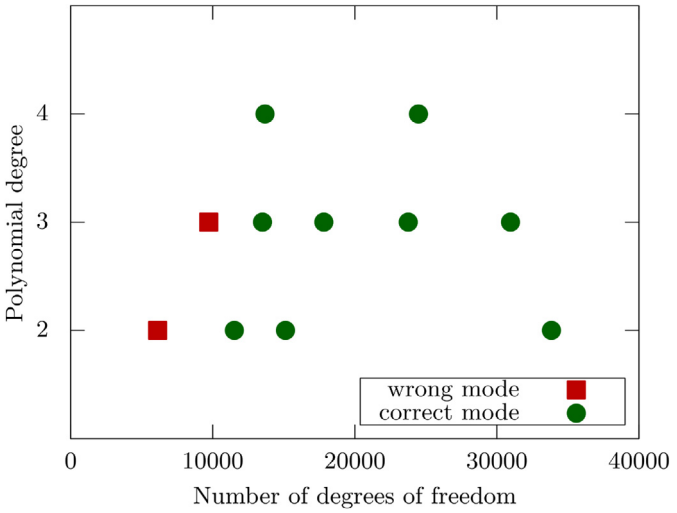


**Fig. 14.** Cylinder with 60 segments: Occurrence of the correct buckling mode for the IGA KL elements. Polynomial degree over number of DOF. Green dots indicate the correct buckling mode, red squares indicate a wrong buckling mode.

For problems with clearly separated critical points, the results obtained with isogeometric analysis do not seem to be superior to results obtained with standard finite elements.

Moreover, the sources of the observed superior accuracy obtained by isogeometric analysis have been investigated systematically. The problem setups were selected in a specific way in order to systematically separate the influence of exact geometry from the influence of the shape functions. The numerical results indicate that the driving force for superior accuracy of IGA over standard finite elements is the high approximation power of $k$-refined NURBS rather than the exact geometry representation. By artificially introducing an intentional geometry error within the segmented cylinder problem setup in both IGA and standard finite element analysis, we demonstrated that a certain level of geometry approximation is sufficient to achieve correct buckling modes.

The studies in this paper are restricted to linear pre-buckling analyses of shells. The results suggest several extensions and future research. Current investigations focus on nonlinear static and dynamic simulations and a more detailed study on the effects of smoothness, polynomial degree and locking on the accuracy.

## Declaration of competing interest

The authors declare the following financial interests/personal relationships which may be considered as potential competing interests: Bastan Oesterle reports financial support was provided by German Research Foundation. Manfred Bischoff reports financial support was provided by German Research Foundation.

## Acknowledgments

This project is supported by the Deutsche Forschungsgemeinschaft (DFG, German Research Foundation) under Grant OE 728/1-1 — 428725889, under Germany's Excellence Strategy – EXC 2120/1 – 390831618 and under Collaborative Research Center 1244 — 279064222. This support is gratefully acknowledged.

## Appendix

See Tables 2–8.

**Table 2**
Cylindrical shell, SHELL63: Number of segments, associated number of DOF, critical load factor $\lambda_{crit}$ and indication whether the correct buckling mode occurred.

| Segments | DOF | $\lambda_{crit}$ | Correct mode |
|---|---|---|---|
| 26 | 43680 | 420.4 | no |
| | 93600 | 422.8 | no |
| | 265200 | 424.3 | no |
| | 374400 | 424.5 | no |
| | 585000 | 424.7 | no |
| 45 | 43200 | 800.9 | no |
| | 97200 | 825.6 | no |
| | 270000 | 836.0 | no |
| | 388800 | 837.3 | no |
| | 567000 | 838.5 | no |
| 52 | 42120 | 815.5 | no |
| | 93600 | 835.1 | no |
| | 249600 | 850.7 | no |
| | 374400 | 853.5 | no |
| | 608400 | 855.5 | no |
| 60 | 43200 | 808.8 | no |
| | 86400 | 838.6 | no |
| | 252000 | 855.7 | no |
| | 388800 | 858.5 | no |
| | 514800 | 860.0 | no |
| | 594000 | 860.3 | yes |
| | 682560 | 860.2 | yes |
| | 721440 | 860.3 | yes |
| 90 | 43200 | 807.0 | no |
| | 97200 | 840.3 | no |
| | 270000 | 857.5 | no |
| | 388800 | 860.3 | yes |
| | 517860 | 860.3 | yes |
| | 567000 | 860.5 | yes |
| 120 | 43200 | 773.2 | no |
| | 86400 | 838.1 | no |
| | 237600 | 858.2 | no |
| | 288000 | 856.9 | no |
| | 345600 | 859.6 | no |
| | 417600 | 859.3 | no |
| | 450000 | 860.1 | yes |
| | 493200 | 860.3 | yes |
| | 648000 | 860.2 | yes |
| $\infty$ | 5760 | 591.8 | no |
| (exact) | 10080 | 674.9 | no |
| | 23040 | 763.3 | no |
| | 40320 | 805.0 | no |
| | 90720 | 837.5 | no |
| | 142200 | 848.1 | no |
| | 252000 | 856.0 | no |
| | 362880 | 858.9 | no |
| | 568800 | 860.2 | yes |
| | 1451520 | 860.3 | yes |

**Table 3**
Cylindrical shell, SHELL181R: Number of segments, associated number of DOF, critical load factor $\lambda_{crit}$ and indication whether the correct buckling mode occurred.

| Segments | DOF | $\lambda_{crit}$ | Correct mode |
|---|---|---|---|
| 26 | 43680 | 440.6 | no |
| | 93600 | 431.4 | no |
| | 265200 | 425.5 | no |
| | 374400 | 424.5 | no |
| | 585000 | 423.5 | no |
| 45 | 43200 | 859.5 | no |
| | 97200 | 851.7 | no |
| | 270000 | 843.5 | no |
| | 388800 | 841.7 | no |
| | 567000 | 840.6 | no |
| 52 | 42120 | 871.4 | no |
| | 93600 | 863.4 | no |
| | 249600 | 859.5 | no |
| | 374400 | 858.8 | no |
| | 608400 | 857.8 | no |
| 60 | 43200 | 873.2 | no |
| | 86400 | 866.6 | no |
| | 252000 | 864.4 | no |
| | 388800 | 863.9 | no |
| | 594000 | 863.5 | no |
| 90 | 43200 | 868.6 | no |
| | 97200 | 866.7 | no |
| | 270000 | 866.4 | no |
| | 388800 | 865.8 | yes |
| | 414720 | 865.8 | yes |
| | 517860 | 864.4 | yes |
| | 567000 | 864.5 | yes |
| 120 | 43200 | 868.4 | no |
| | 86400 | 865.9 | no |
| | 237600 | 865.9 | no |
| | 345600 | 865.9 | no |
| | 417600 | 864.9 | yes |
| | 450000 | 864.9 | yes |
| | 493200 | 864.9 | yes |
| | 648000 | 863.7 | yes |
| $\infty$ | 5760 | 881.6 | no |
| (exact) | 10080 | 872.5 | no |
| | 23040 | 868.3 | no |
| | 40320 | 868.0 | no |
| | 90720 | 868.3 | no |
| | 142200 | 866.1 | no |
| | 252000 | 865.8 | no |
| | 362880 | 865.4 | no |
| | 568800 | 864.8 | yes |
| | 1451520 | 862.5 | yes |

**Table 4**
Cylindrical shell, SHELL181F: Number of segments, associated number of DOF, critical load factor $\lambda_{crit}$ and indication whether the correct buckling mode occurred.

| Segments | DOF | $\lambda_{crit}$ | Correct mode |
|---|---|---|---|
| 26 | 43680 | 436.6 | no |
| | 93600 | 429.5 | no |
| | 265200 | 424.8 | no |
| | 374400 | 423.9 | no |
| | 585000 | 423.2 | no |
| 45 | 43200 | 891.3 | no |
| | 97200 | 861.6 | no |
| | 270000 | 846.1 | no |
| | 388800 | 843.5 | no |
| | 567000 | 841.8 | no |
| 52 | 42120 | 910.7 | no |
| | 93600 | 879.8 | no |
| | 249600 | 864.9 | no |
| | 374400 | 861.6 | no |
| | 608400 | 859.2 | no |
| 60 | 43200 | 905.9 | no |
| | 86400 | 885.2 | no |
| | 252000 | 868.2 | yes |
| | 311040 | 866.3 | yes |
| | 388800 | 864.9 | yes |
| | 493200 | 864.0 | yes |
| | 594000 | 863.4 | yes |
| 90 | 43200 | 903.8 | no |
| | 97200 | 879.8 | yes |
| | 270000 | 867.4 | yes |
| | 388800 | 865.3 | yes |
| | 567000 | 864.1 | yes |
| 120 | 43200 | 890.8 | no |
| | 86400 | 882.9 | no |
| | 237600 | 870.5 | yes |
| | 345600 | 866.4 | yes |
| | 432000 | 864.5 | yes |
| | 648000 | 863.4 | yes |
| $\infty$ | 5760 | 1119.3 | no |
| (exact) | 10080 | 1006.1 | no |
| | 23040 | 927.7 | no |
| | 40320 | 901.4 | no |
| | 90720 | 880.4 | no |
| | 142200 | 873.9 | yes |
| | 252000 | 868.3 | yes |
| | 362880 | 866.1 | yes |
| | 568800 | 864.2 | yes |
| | 1451520 | 862.3 | yes |

**Table 5**
Cylindrical shell, SHELL281: Number of segments, associated number of DOF, critical load factor $\lambda_{crit}$ and indication whether the correct buckling mode occurred.

| Segments | DOF | $\lambda_{crit}$ | Correct mode |
|---|---|---|---|
| 26 | 28080 | 434.0 | no |
| | 70200 | 421.2 | no |
| | 131040 | 420.6 | no |
| | 280800 | 420.3 | no |
| | 795600 | 423.5 | no |
| 45 | 32400 | 863.4 | no |
| | 72900 | 841.3 | no |
| | 129600 | 837.5 | no |
| | 291600 | 836.5 | no |
| | 810000 | 836.5 | no |
| 52 | 29952 | 867.1 | no |
| | 67392 | 859.6 | no |
| | 126360 | 855.8 | no |
| | 280800 | 854.7 | no |
| | 748800 | 854.7 | no |
| 60 | 29160 | 870.8 | no |
| | 66960 | 861.4 | yes/no[a] |
| | 129600 | 859.4 | yes |
| | 259200 | 858.9 | yes |
| | 557280 | 858.9 | yes |
| | 756000 | 858.9 | yes |
| 90 | 32400 | 871.2 | no |
| | 68040 | 861.3 | yes |
| | 129600 | 860.1 | yes |
| | 291600 | 859.7 | yes |
| | 557280 | 859.7 | yes |
| | 810000 | 859.7 | yes |
| 120 | 43200 | 865.2 | no |
| | 64800 | 861.9 | yes |
| | 129600 | 859.9 | yes |
| | 259200 | 859.9 | yes |
| | 712800 | 859.8 | yes |
| $\infty$ | 5832 | 875.8 | no |
| (exact) | 17280 | 865.1 | no |
| | 30240 | 865.8 | no |
| | 69120 | 861.9 | yes |
| | 120960 | 860.8 | yes |
| | 272160 | 860.5 | yes |
| | 426600 | 860.4 | yes |
| | 756000 | 860.4 | yes |
| | 1088640 | 860.4 | yes |

[a]Number of halfwaves in hoop direction is correct, in axial direction, the upper and lower most halfwaves are not very well pronounced.

**Table 6**
Cylindrical shell, IGA KL $p = 2$: Number of segments, associated number of DOF, critical load factor $\lambda_{crit}$ and indication whether the correct buckling mode occurred.

| Segments | DOF | $\lambda_{crit}$ | Correct mode |
|---|---|---|---|
| 60 | 6120 | 897.7 | no |
| | 11520 | 887.2 | yes |
| | 15120 | 885.1 | yes |
| | 33840 | 874.7 | yes |
| $\infty$ | 3060 | 941.9 | no |
| (exact) | 5280 | 897.4 | yes |
| | 11880 | 871.8 | yes |
| | 20640 | 866.3 | yes |
| | 31800 | 864.1 | yes |
| | 46080 | 863.0 | yes |

**Table 7**
Cylindrical shell, IGA KL $p = 3$: Number of segments, associated number of DOF, critical load factor $\lambda_{crit}$ and indication whether the correct buckling mode occurred.

| Segments | DOF | $\lambda_{crit}$ | Correct mode |
|---|---|---|---|
| 60 | 9720 | 873.4 | no |
| | 13500 | 872.7 | yes |
| | 17820 | 872.6 | yes |
| | 23760 | 861.6 | yes |
| | 30960 | 861.5 | yes |
| $\infty$ | 3456 | 870.6 | yes |
| (exact) | 5796 | 862.2 | yes |
| | 12648 | 860.8 | yes |
| | 21648 | 860.7 | yes |
| | 33048 | 860.7 | yes |

**Table 8**
Cylindrical shell, IGA KL $p = 4$: Number of segments, associated number of DOF, critical load factor $\lambda_{crit}$ and indication whether the correct buckling mode occurred.

| Segments | DOF | $\lambda_{crit}$ | Correct mode |
|---|---|---|---|
| 60 | 13680 | 860.9 | yes |
| | 24480 | 860.8 | yes |
| $\infty$ | 3876 | 861.9 | yes |
| (exact) | 6336 | 860.8 | yes |
| | 13440 | 860.7 | yes |
| | 20640 | 860.7 | yes |

## References

[1] F. Cirak, M. Ortiz, P. Schröder, Subdivision surfaces: a new paradigm for thin-shell finite-element analysis, Internat. J. Numer. Methods Engrg. 47 (12) (2000) 2039–2072, http://dx.doi.org/10.1002/(SICI)1097-0207(20000430)47:12<2039::AID-NME872>3.0.CO;2-1.

[2] J. Kiendl, K.U. Bletzinger, J. Linhard, R. Wüchner, Isogeometric shell analysis with Kirchhoff–love elements, Comput. Methods Appl. Mech. Engrg. 198 (49–52) (2009) 3902–3914, http://dx.doi.org/10.1016/j.cma.2009.08.013.

[3] D.J. Benson, Y. Bazilevs, M.C. Hsu, T.J.R. Hughes, Isogeometric shell analysis: The Reissner–Mindlin shell, Computational Geometry and Analysis, Comput. Methods Appl. Mech. Engrg. 199 (5) (2010) 276–289, http://dx.doi.org/10.1016/j.cma.2009.05.011, URL http://www.sciencedirect.com/science/article/pii/S0045782509001820.

[4] D.J. Benson, Y. Bazilevs, M.C. Hsu, T.J.R. Hughes, A large deformation, rotation-free, isogeometric shell, Comput. Methods Appl. Mech. Engrg. 200 (13–16) (2011) 1367–1378, http://dx.doi.org/10.1016/j.cma.2010.12.003.

[5] Q. Long, P. Burkhard Bornemann, F. Cirak, Shear-flexible subdivision shells, Internat. J. Numer. Methods Engrg. 90 (13) (2012) 1549–1577, http://dx.doi.org/10.1002/nme.3368.

[6] R. Echter, B. Oesterle, M. Bischoff, A hierarchic family of isogeometric shell finite elements, Comput. Methods Appl. Mech. Engrg. 254 (2013) 170–180, http://dx.doi.org/10.1016/j.cma.2012.10.018.

[7] D.J. Benson, S. Hartmann, Y. Bazilevs, M.C. Hsu, T.J.R. Hughes, Blended isogeometric shells, Comput. Methods Appl. Mech. Engrg. 255 (2013) 133–146, http://dx.doi.org/10.1016/j.cma.2012.11.020.
[8] W. Dornisch, S. Klinkel, B. Simeon, Isogeometric Reissner–Mindlin shell analysis with exactly calculated director vectors, Comput. Methods Appl. Mech. Engrg. 253 (2013) 491–504, http://dx.doi.org/10.1016/j.cma.2012.09.010.
[9] B. Oesterle, E. Ramm, M. Bischoff, A shear deformable, rotation-free isogeometric shell formulation, Comput. Methods Appl. Mech. Engrg. 307 (2016) 235–255, http://dx.doi.org/10.1016/j.cma.2016.04.015.
[10] T.J.R. Hughes, J.A. Cottrell, Y. Bazilevs, Isogeometric analysis: CAD, finite elements, NURBS, exact geometry and Mesh refinement, Comput. Methods Appl. Mech. Engrg. 194 (39–41) (2005) 4135–4195, http://dx.doi.org/10.1016/j.cma.2004.10.008.
[11] S. Morganti, F. Auricchio, D.J. Benson, F.I. Gambarin, S. Hartmann, T.J.R. Hughes, A. Reali, Patient-specific isogeometric structural analysis of aortic valve closure, Isogeometric Analysis Special Issue, Comput. Methods Appl. Mech. Engrg. 284 (2015) 508–520, http://dx.doi.org/10.1016/j.cma.2014.10.010.
[12] J.A. Cottrell, T.J.R. Hughes, A. Reali, Studies of refinement and continuity in isogeometric structural analysis, Comput. Methods Appl. Mech. Engrg. 196 (41) (2007) 4160–4183, http://dx.doi.org/10.1016/j.cma.2007.04.007.
[13] C. Adam, S. Bouabdallah, M. Zarroug, H. Maitournam, Improved numerical integration for locking treatment in isogeometric structural elements, part I: Beams, Comput. Methods Appl. Mech. Engrg. 279 (2014) 1–28, http://dx.doi.org/10.1016/j.cma.2014.06.023.
[14] C. Adam, S. Bouabdallah, M. Zarroug, H. Maitournam, Improved numerical integration for locking treatment in isogeometric structural elements. part II: Plates and shells, Isogeometric Analysis Special Issue, Comput. Methods Appl. Mech. Engrg. 284 (2015) 106–137, http://dx.doi.org/10.1016/j.cma.2014.07.020.
[15] S. Bieber, B. Oesterle, E. Ramm, M. Bischoff, A variational method to avoid locking—Independent of the discretization scheme, Internat. J. Numer. Methods Engrg. 114 (8) (2018) 801–827, http://dx.doi.org/10.1002/nme.5766.
[16] L. Leonetti, D. Magisano, F. Liguori, G. Garcea, An isogeometric formulation of the Koiter's theory for buckling and initial post-buckling analysis of composite shells, Comput. Methods Appl. Mech. Engrg. 337 (2018) 387–410, http://dx.doi.org/10.1016/j.cma.2018.03.037.
[17] Y. Guo, H. Do, M. Ruess, Isogeometric stability analysis of thin shells: From simple geometries to engineering models, Internat. J. Numer. Methods Engrg. 118 (8) (2019) 433–458, http://dx.doi.org/10.1002/nme.6020.
[18] O.C. Zienkiewicz, R.L. Taylor, The Finite Element Method, fourth ed. McGraw-Hill.
[19] C.A. Felippa, Nonlinear finite element methods (ASEN 6107), lecture notes, 2016, Boulder, Colorado 80309-0429, USA: University of Colorado.
[20] E. Riks, The application of Newton's method to the problem of elastic stability, J. Appl. Mech. 39 (4) (1972) 1060–1065, http://dx.doi.org/10.1115/1.3422829.
[21] E. Riks, An incremental approach to the solution of snapping and buckling problems, Int. J. Solids Struct. 15 (7) (1979) 529–551, http://dx.doi.org/10.1016/0020-7683(79)90081-7.
[22] M.A. Crisfield, A fast incremental/iterative solution procedure that handles "snap-through", Comput. Struct. 13 (1) (1981) 55–62, http://dx.doi.org/10.1016/0045-7949(81)90108-5.
[23] E. Ramm, Strategies for tracing the nonlinear response near limit points, in: Nonlinear Finite Element Analysis in Structural Mechanics, Springer, Berlin, Heidelberg, pp. 63–89, http://dx.doi.org/10.1007/978-3-642-81589-8_5.
[24] K.H. Schweizerhof, P. Wriggers, Consistent linearization for path following methods in nonlinear fe analysis, Comput. Methods Appl. Mech. Engrg. 59 (3) 261–279, http://dx.doi.org/10.1016/0045-7825(86)90001-0.
[25] J.-L. Batoz, G. Dhatt, Incremental displacement algorithms for nonlinear problems, Internat. J. Numer. Methods Engrg. 14 (8) 1262–1267, http://dx.doi.org/10.1002/nme.1620140811.
[26] R. Seydel, Numerical computation of branch points in ordinary differential equations, Numer. Math. 32 (1) (1979) 51–68, http://dx.doi.org/10.1007/BF01397649.
[27] P. Wriggers, W. Wagner, C. Miehe, A quadratically convergent procedure for the calculation of stability points in finite element analysis, Comput. Methods Appl. Mech. Engrg. 70 (3) (1988) 329–347, http://dx.doi.org/10.1016/0045-7825(88)90024-2.
[28] P. Wriggers, J.C. Simo, A general procedure for the direct computation of turning and bifurcation points, Internat. J. Numer. Methods Engrg. 30 (1) (1990) 155–176, http://dx.doi.org/10.1002/nme.1620300110.
[29] P. Wriggers, Nichtlineare Finite-Element-Methoden, Springer, 2001.
[30] B. Oesterle, R. Sachse, E. Ramm, M. Bischoff, Hierarchic isogeometric large rotation shell elements including linearized transverse shear parametrization, Comput. Methods Appl. Mech. Engrg. 321 (2017) 383–405, http://dx.doi.org/10.1016/j.cma.2017.03.031.
[31] J. Kiendl, Y. Bazilevs, M.C. Hsu, R. Wüchner, K.U. Bletzinger, The bending strip method for isogeometric analysis of Kirchhoff–love shell structures comprised of multiple patches, Comput. Methods Appl. Mech. Engrg. 199 (37–40) (2010) 2403–2416, http://dx.doi.org/10.1016/j.cma.2010.03.029.
[32] R. Lehoucq, D. Sorensen, C. Yang, C. Manschoff, ARPACK++ c++ interface to ARPACK cod v1.2 2/20/2000 URL http://www.caam.rice.edu/software/ARPACK/,
[33] F.M. Gomes, D.C. Sorensen, ARPACK++ c++ user's guide 1.2- May 1, 2000 URL http://www.caam.rice.edu/software/ARPACK/.
[34] D.C. Sorensen, Implicitly restarted arnoldi/lanczos methods for large scale eigenvalue calculations, in: Parallel Numerical Algorithms, in: ICASE/LaRC Interdisciplinary Series in Science and Engineering, Springer, Dordrecht, pp. 119–165, http://dx.doi.org/10.1007/978-94-011-5412-3_5.
[35] J.A. Stricklin, W.E. Haisler, P.R. Tisdale, R. Gunderson, A rapidly converging triangular plate element, AIAA J. 7 (1) (1969) 180–181, http://dx.doi.org/10.2514/3.5068.
[36] G.S. Dhatt, An efficient triangular shell element, AIAA J. 8 (11) (1970) 2100–2102, http://dx.doi.org/10.2514/3.6068.
[37] J.-L. Batoz, K.-J. Bathe, L.-W. Ho, A study of three-node triangular plate bending elements, Internat. J. Numer. Methods Engrg. 15 (12) (1980) 1771–1812, http://dx.doi.org/10.1002/nme.1620151205.

[38] J.-L. Batoz, An explicit formulation for an efficient triangular plate-bending element, Internat. J. Numer. Methods Engrg. 18 (7) (1982) 1077–1089, http://dx.doi.org/10.1002/nme.1620180711.
[39] R.L. Taylor, P.J. Beresford, E.L. Wilson, A non-conforming element for stress analysis, Internat. J. Numer. Methods Engrg. 10 (6) (1976) 1211–1219, http://dx.doi.org/10.1002/nme.1620100602.
[40] T.J.R. Hughes, T.E. Tezduyar, Finite elements based upon mindlin plate theory with particular reference to the four-node bilinear isoparametric element, J. Appl. Mech. 48 (3) (1981) 587–596, http://dx.doi.org/10.1115/1.3157679.
[41] ANSYS 18.0 Documentation ANSYS Inc.
[42] L.H. Donnell, Beams, Plates and Shells, McGraw-Hill, 1976.